Growth and collapse of nanovoids in tantalum monocrystals

Yizhe Tang [a], Eduardo M. Bringa [b], Bruce A. Remington [c], Marc A. Meyers [a,*]

[a] *University of California, San Diego, La Jolla, CA 92093, USA*
[b] *CONICET & Instituto de Ciencias Básicas, Univ. Nac.Cuyo, Mendoza 5500, Argentina*
[c] *Lawrence Livermore National Laboratory, Livermore, CA 94550, USA*

Abstract

The growth and collapse of nanoscale voids are investigated for tantalum (a model body-centered cubic metal) under different stress states and strain rates by molecular dynamics (MD). Three principal mechanisms of deformation are identified and quantitatively evaluated: (i) shear loop emission and subsequent expansion from the surface of the void; (ii) cooperative shear loop emission from slip planes that are parallel to the same $\langle 1\,1\,1 \rangle$ slip direction and their combination, forming prismatic loops; (iii) twinning starting at the void surface. The generation and evolution of these defects are found to be functions of stress state and strain rate. Dislocations are found to propagate preferably on $\{1\,1\,0\}$ and $\{1\,1\,2\}$ planes, with Burgers vectors $1/2\,\langle 1\,1\,1 \rangle$. The dislocation shear loops generated expand in a crystallographic manner, and in hydrostatic tension and compression generate prismatic loops that detach from the void. In uniaxial tensile strain along [1 0 0], the extremities of the shear loops remain attached to the void surface, a requisite for void growth. In uniaxial compressive strain, the extremities of the shear loops can also detach from the void surface. The difference in defect evolution is explained by the equal resolved shear stress in the hydrostatic loading case, in contrast with uniaxial strain loading. Nanotwins form preferably upon both uniaxial tensile strain and hydrostatic stress (in tension) and there is a slip-to-twinning transition as the strain rate exceeds $10^8\,\text{s}^{-1}$. A simplified constitutive description is presented which explains the preponderance of twinning over slip in tension beyond a critical strain rate. The formation of both dislocations and twins is confirmed through laser compression experiments, which provide strain rates ($\sim 10^8\,\text{s}^{-1}$) comparable to MD. The dislocation velocities are determined by tracking the edge component of the expanding loops and are found to be subsonic even at extremely high stress and strain rates: $680\,\text{m s}^{-1}$ for $10^8\,\text{s}^{-1}$ and $1020\,\text{m s}^{-1}$ for $10^9\,\text{s}^{-1}$.

© 2010 Acta Materialia Inc. Published by Elsevier Ltd. All rights reserved.

Keywords: Molecular dynamics; Void growth; Shear loops

1. Introduction

The nucleation, growth and coalescence of voids lead to ductile fracture of metals. One of the first to realize this phenomenon was Tipper in 1949 [1]. A complete account of this is given by Dodd and Bai [2]. Although a number of continuum models for the growth of voids have been proposed [3–6], the atomistic mechanisms are still not completely understood. There has been a common but unsubstantiated belief that the initiation of void formation

takes place by vacancy diffusion in pure monocrystalline metals. This will be discussed in Section 2. An alternative approach, based on dislocation, is discussed first, in this section.

The early dislocation-based models have inherent weaknesses. Stevens et al. [7] proposed a dislocation-based model for growth of voids, in which the void is a sink of dislocations. In the model proposed by Meyers and Aimone [8], intersecting dislocations diverging from a point were considered. A model of void growth by emission of prismatic loops was proposed by Wolfer [9] to treat porosity and plasticity in radiation-damaged materials and has been adopted by Ahn et al. [10] to explain and model spalling in aluminum. An analytical model was proposed by

Lubarda et al. [11] based on the emission of both prismatic and shear loops, with mechanisms analogous to the Ashby [12,13] theory for the generation of geometrically necessary dislocations in the deformation of plastically inhomogeneous materials.

There has been considerable effort in the modeling of void growth by molecular dynamics. We highlight here the contributions most relevant to the current investigation. Simultaneously with the proposal of Lubarda et al. [11], several molecular dynamics contributions revealed the initiation and propagation of these loops. Seppälä et al. [14–16] studied void growth in several papers, without focusing on dislocation analysis. Traiviratana et al. [17,18] observed the emission of shear loops in a face-centered cubic metal (copper) subjected to uniaxial tensile strain. Marian et al. [19,20] carried out quasi-continuum (QC) calculations which showed the formation of shear loops in aluminum subjected to simple shear. Dávila et al. [21] carried out molecular dynamics (MD) simulations of void collapse in copper subjected to shock compression, and found that the emission of loops was responsible for the collapse of voids. Zhu et al. [22] modeled void growth during release of shock loading in a face-centered cubic (fcc) metal (copper); shear dislocation loop emission from the equator of the void under [1 0 0] loading was observed. Detailed MD calculations by Bringa et al. [23] confirmed that shear loop emission is the principal mechanism of void growth in copper; the effects of void size and load orientation were found to be significant, and one-, two- and three-dimensional loop arrangements were identified and analyzed. Subsequent to the discussion by Bulatov et al. [24] on the impossibility of void growth by shear, Bringa et al. [25] analyzed the previous results critically and demonstrated that the shear loops have to stay attached to the void surface to allow growth.

Void growth in polycrystalline copper, modeled by a nanocrystalline structure, was simulated by Rudd and Belak [26]. They observed the initiation of voids at grain boundaries and grain-boundary triple points. Dongare et al. [27] conducted a detailed analysis of void formation in nanocrystalline metals with small grain size, while behavior for a larger grain size (but still in the nanometer range) was analyzed by Traiviratana et al. [17] and Bringa et al. [23].

Efforts have also been made to reveal the void growth mechanisms in body-centered cubic (bcc) metals. The contribution by Rudd [28] represents the most significant effort. He carried out a detailed analysis of void growth in V, Nb, Mo, Ta and W; these simulations were all carried out using Finnis–Sinclair potentials [29] and in hydrostatic tension. Prismatic loops were observed, and a slip-to-twinning transition was also observed when the strain rate increased. Recently, Marian et al. [30] also extended the QC calculations to void (10.9 nm diameter) collapse in a bcc metal (tantalum) under uniaxial loading along [0 0 1] and [$\bar{4}$ 8 1 9] directions. Loop generation (loading in [0 0 1]) at the void surface and twinning (loading in [$\bar{4}$ 8 1 9]) were observed.

Body-centered cubic metals exhibit an asymmetry (in tension vs. compression) in the flow stress, which is absent in fcc metals. This phenomenon has been studied extensively by Vitek and co-workers [31–34] and Seeger [35], and is attributed to dislocation core effects. Thus, the growth and collapse of voids can be affected by this asymmetry.

The goal of the current investigation is to extend the study by Bringa et al. [23] to a bcc metal and to rationalize the recent results by Rudd [28] by developing a mechanistic understanding of the deformation mechanisms. In order to accomplish this goal, two parameters were systematically varied: (i) stress state and (ii) strain rate.

2. Void initiation mechanisms

The void initiation process in pure monocrystals has often been assumed to be governed by the diffusion of vacancies towards a central point, creating and nourishing a void. Thus, one can envisage the convergent flow of vacancies to a specific point, forming a void. One of the most rapid diffusion mechanisms is "pipe" diffusion, in which vacancies migrate along dislocation lines. Indeed, this was suggested by Cuitiño and Ortiz [36] based on an enhanced vacancy concentration created by plastic deformation principally through multiple glide and dislocation intersection. The vacancy concentration generated by plastic deformation has been proposed by Seitz [37] and Mott [38–40] to vary linearly with strain ε (a term accounting for the equilibrium concentration has been added here):

$$c_0 \approx 10^{-4}\varepsilon + c_{eq} = 10^{-4}\varepsilon + \exp\left(\frac{-Q}{k_B T}\right) \qquad (1)$$

where c_{eq} is the equilibrium vacancy concentration, Q is the activation energy for the formation of a vacancy, k_B is the Boltzmann constant and T is the temperature. Although there are alternative expressions, this will suffice for the present calculation. Cuitiño and Ortiz [36] developed a specific mechanism for this mode of vacancy diffusion, with the following equation predicting the time change of void radius, R, in terms of the pipe diffusion coefficient, D,

$$\frac{dR}{dt} = \frac{1}{R}D(c_0 - c_s) \qquad (2)$$

$$c_s = c_{eq}\exp\left(\frac{2\gamma V_v}{Rk_B T}\right) = \exp\left(\frac{2\gamma V_v/R - Q}{k_B T}\right) \qquad (3)$$

where c_0 is the void concentration due to plastic deformation, c_s is the vacancy concentration at the surface of the void, γ is the surface energy, and V_v is the atomic volume.

If one assumes that void initiation takes place at $\varepsilon = 1$, it is safe to assume $c_0 \gg c_s$. One obtains, from Eq. (1) ($\varepsilon = 1$, $Q = 4.48 \times 10^{-19}$ J from experimental data for tantalum [41], $T = 300$ K), $c_0 \sim 10^{-4}$.

From Eq. (3) one obtains c_s, the vacancy concentration at the surface of the void ($\gamma = 2.68$ J m^{-2} from experimental data for tantalum [42], $V_v = 4\pi/3 \times (0.143 \text{ nm})^3$, $R = 2 \times 0.143$ nm, $T = 300$ K): $c_s \sim 1.0 \times 10^{-23}$.

Integrating Eq. (2) yields:

$$\frac{R}{R_0} = \left(1 + \frac{2Dc_0}{R_0^2}t\right)^{1/2} \tag{4}$$

where t is the time in seconds. The initial void radius, R_0, was taken as the atomic radius for tantalum, 0.143 nm. Values of diffusion coefficient D at different temperatures are taken from experimental data for tantalum [43]. The normalized void radius R/R_0 vs. time at three different temperatures is shown in Fig. 1. Conventional plastic deformation at a conservative strain rate $10^{-2}\,s^{-1}$ will lead to a failure time of 10^2 s assuming a strain of 1. Failure is typically characterized by voids with radii ranging in the micrometers ($R/R_0 \sim 10^4$); this is the typical dimple size in fracture surfaces. The times predicted by Eq. (4) at 1260 K are longer by many orders of magnitude ($>10^{10}$ s). Even at nearly 2000 K, voids will require 10^5 s to grow to a radius of 0.1 μm. Thus, vacancy diffusion, which is the principal mechanism of void growth in creep fracture, as treated by Raj and Ashby [44], cannot be the operating mechanism in conventional plastic deformation of tantalum. This mechanism was also discounted for copper deformed at conventional strain rates at ambient temperature [18].

Most engineering alloys are polycrystalline and contain second-phase particles. It is well known that inclusions serve as initiation sites for voids either by separation of the interface or by their fracture during plastic deformation [45–47], forming an initial void of size equivalent to the particle. The presence of second phases has a profound effect on the total elongation, as expressed by Fig. 2, based on measurements on a number of copper-based alloys with dispersions of different sizes and fractions [48]. The fracture strain increases exponentially as purity is increased. In the extreme case when no nucleation sites (other than vacancies) are present, the fracture strain tends to infinity and the fracture mode has been called "rupture" by Chin et al. [49] and "knife-edge" by others [50]. Broek [51] presents a schematic showing how the sequential activation
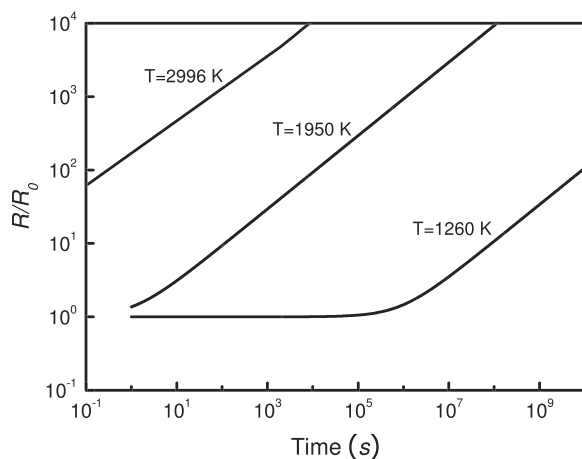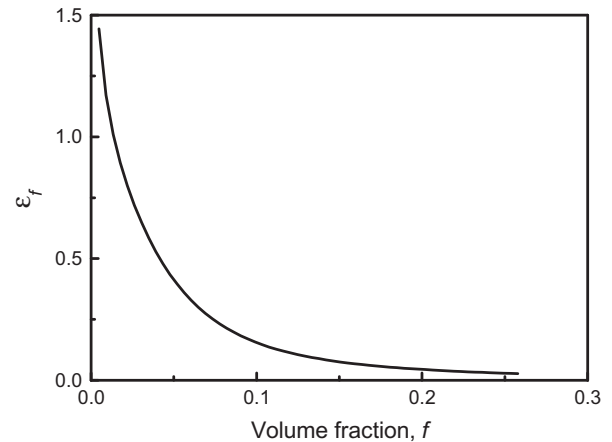

Fig. 2. Tensile ductility (true strain in the neck at fracture) ε_f as a function of volume fraction f, for various second-phase particles copper alloys (adapted from Edelson and Baldwin [48]).

of two slip planes leads to a sharp fracture in which the cross-sectional area is reduced to nearly zero.

The ubiquitous observation of voids nucleating at second-phase particles and the difficulty of associated with homogeneous nucleation have led to a consensus that, in pure monocrystals, fracture does not involve the nucleation, growth and coalescence of voids. Two important factors counter this argument:

(a) In shock compression experiments, the reflected tensile pulse is known to create spalling by the nucleation–growth–coalescence sequence even in high-purity monocrystals [52]. The unique stress state (uniaxial strain) created by the reflected pulse does not allow the tensile instability and therefore spalling is initiated internally. Concurrent with this, the stress required for spalling in monocrystals is higher than in polycrystals and in metals containing second-phase particles.

(b) The results by Rosi and Abrahams [53] on [1 0 0] Cu, Ag and Cu–0.1% Al single crystals pulled in tension and characterized under the fracture regions revealed voids in their proximity. The fracture was either knife-edge or V-shaped, and the reduction in area was nearly 100%. Fig. 3 shows a schematic of specimen as well as the micrographs showing voids. It is clear that voids formed in the vicinity of the fracture, although it is of the "knife-edge" or "rupture" type. The voids are indicated by arrows.

These results are indeed significant and indicate the possibility of voids nucleating and growing in pure monocrystals by dislocation-based mechanisms. The molecular dynamics component of this investigation will model this phenomenon for tantalum.

3. Computational methods

The molecular dynamics LAMMPS (large-scale atomic/molecular massively parallel simulator) [54] code was used

Fig. 1. Increase in normalized radius R/R_0 of void for tantalum by vacancy diffusion as a function of time.
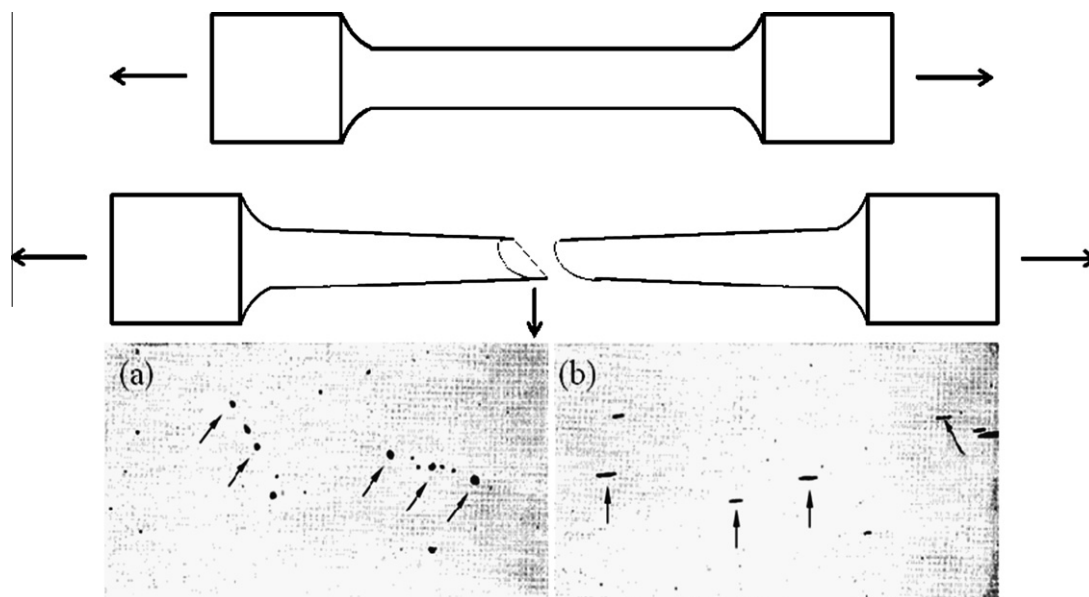
Fig. 3. Appearance of voids in section near and parallel to the fracture surface in: (a) Cu; (b) Ag single crystal (adapted from Rosi and Abrahams [53], fig. 2a and b).

in this investigation. For the bcc tantalum structure, the extended Finnis–Sinclair potential by Dai et al. [55] was used. Unlike the Finnis–Sinclair potential [29,56], which shows artificial behavior at high pressure (see Fig. 1e in Ref. [55]), this potential can still give the correct volume–pressure relation at pressures up to 500 GPa [57]. The number of atoms was 2×10^6. Calculations were performed on parallel PCs and on the TeraGrid supercomputer.

The single crystal tantalum domain was a cube with a spherical void at the center. The void radius R is 3.3 nm. Box size was $100 \times 100 \times 100$ unit cells. Periodic boundaries were applied in all directions. The different domains were subjected to a uniform stress state by re-scaling of the atomic coordinates. These states included uniaxial tensile and compressive strain along [1 0 0], and triaxial (hydrostatic) tensile and compressive strain along [1 0 0], [0 1 0] and [0 0 1]. All simulations were done at an initial temperature of 300 K. The strain rate varied from 10^8 to $10^9 \, \mathrm{s^{-1}}$. All samples were equilibrated to reach zero pressure and the desired initial temperature. Loading was carried out without any temperature control, to capture temperature effects related to plasticity. Visualization of stacking faults, partial and full dislocations, twin boundaries and free surfaces was conducted in visual molecular dynamics [58] with a filter using common neighbor analysis [59]. Filtering with the centro-symmetry parameter (CSP) [60] resulted in similar results when the second neighbor shell was used in the CSP calculation, following the suggestion by Rudd [28].

The generalized stacking fault energies for {1 1 0}, {1 1 2} and {1 2 3} slip planes were calculated using molecular statics, using conjugate gradient in LAMMPS. For each slip plane, periodic boundaries were applied in directions parallel to the slip plane of a 24 nm cubic crystal, and only relaxations along the slip direction of the generalized fault were not allowed; hence the crystal was free to move

along the two directions perpendicular to the slip direction of the fault.

4. Results and discussion

This section is divided into eight parts. First, the different parameters (stress state and strain rate) investigated are briefly presented, with an overview of the simulations carried out. Sections 4.2–4.4 discuss the three principal deformation mechanisms indentified, respectively:

(a) Shear loop emission and subsequent expansion from the surface of the void.
(b) Cooperative shear loop emission from slip planes that parallel to the same ⟨111⟩ slip direction and their combination, forming triangular or hexagonal prismatic loops.
(c) Twinning starting at the void surface.

Section 4.5 analyzes the effects of the imposed parameters (stress state and strain rate) on the slip-to-twinning transition in terms of constitutive models. In Section 4.6 defects observed in tantalum under deformation conditions approaching, as much as possible, the MD stresses and strain rates are presented. Section 4.7 presents detailed analyses of stacking fault energies for {1 1 0}, {1 1 2} and {1 2 3} slip planes. The dislocation velocities and stresses for dislocation emission are analyzed in Section 4.8.

4.1. Simulation parameters and defect generation and evolution

Conditions under which simulations were performed are hydrostatic stress (tension and compression) and uniaxial strain (tensile and compressive) at both 10^8 and $10^9 \, \mathrm{s^{-1}}$.

Two distinct deformation mechanisms were clearly identified: slip and twinning. These deformation mechanisms in void growth and collapse are summarized in Table 1. Twinning only occurs in tension (both hydrostatic tension and uniaxial tensile strain) at the strain rate of 10^9 s^{-1} while shear loop emission occurs in all other cases. The shear loops form on {1 1 2} (in tension) and {1 1 0} planes (in compression) with Burgers vectors $1/2 \langle 1\,1\,1 \rangle$, as experimentally observed for bcc metals when deformation occurs at low strain rate. The twinning planes are {1 1 2} planes. As these shear loops expand, shear loops emitted from slip planes that are parallel to the same $\langle 1\,1\,1 \rangle$ slip direction can combine and form prismatic loops in some cases (hydrostatic tension and compression). This will be discussed in detail in Sections 4.2–4.4.

We will first present the details of shear loop nucleation. This is shown for a 3.3 nm radius void in hydrostatic tension at strain rate of 10^8 s^{-1} in Fig. 4. Fig. 4a shows the cross-section of the void, and Fig. 4b shows the void surface, that is initially faceted. Fig. 4c shows two {1 1 0} stacking faults, $(\bar{1}10)$ and $(\bar{1}0\bar{1})$, nucleating at the void surface and intersecting it at 45°, the angle at which the shear stresses are maximum. The traces of these two {1 1 0} slip planes are schematically shown in Fig. 4d. After the nucleation of these two {1 1 0} faults, subsequent slip occurs equally and alternatively in these two {1 1 0} planes, forming a {1 1 2} fault, since:

$$(\bar{1}10) + (\bar{1}0\bar{1}) = (\bar{2}1\bar{1})$$

Thus, the microscopic $(\bar{2}1\bar{1})$ plane is composed, at the atomic level, of $(\bar{1}10)$ and $(\bar{1}0\bar{1})$ steps. One can also form other configurations, such as two $(\bar{1}10)$ segments plus one $(\bar{1}0\bar{1})$ segment forming a $(\bar{3}2\bar{1})$ plane, since:

$$2(\bar{1}10) + (\bar{1}0\bar{1}) = (\bar{3}2\bar{1})$$

At the same time, the leading and trailing partials of these {1 1 0} faults always react, leaving a "hole" in the center of this {1 1 2} fault; thus a shear loop lying on {1 1 2} plane is generated, as shown in Fig. 4e and f.

All these planes have a common intersection: $[1\,1\,\bar{1}]$. This is the classic "pencil glide" configuration for slip in bcc metals. The edge components of the dislocation loops advance and move away from the void, while the screw components, being less mobile, stay back as straight segments. The edge component of the dislocation often acquires curvature, outside of the $(\bar{2}1\bar{1})$ plane (as shown in Fig. 4e), because dislocation segments can reside in any of the $(\bar{1}10, (\bar{1}0\bar{1}), (\bar{2}1\bar{1})$ or $(\bar{3}2\bar{1})$ planes. This will be shown later.

4.2. Emission of shear loops

Fig. 5 shows the sequence of defect evolution in uniaxial compressive loading at a strain rate of 10^8 s^{-1}. Emission of a non-planar shear loop lying on {1 1 0} planes is shown in Fig. 5a. As the stress increases, loops are formed on several planes. The edge components of the formed shear loops, with Burgers vector $\mathbf{b} = 1/2 \langle 1\,1\,1 \rangle$, move along $\langle 1\,1\,1 \rangle$ direction while the screw components expand much less

Table 1
Summary of the three mechanisms in void growth and collapse ($R = 3.3$ nm): emission of shear loops (S), emission of prismatic loops (P) and twinning (T).

| Strain rate	Void growth		Void collapse	
	Hydrostatic tension	Uniaxial tensile strain	Hydrostatic compression	Uniaxial compressive strain
10^8 s^{-1}	$S + P$	S (axial symmetry of stress field)	$S + P$	S
10^9 s^{-1}	T (generated by $1/2 \langle 1\,1\,1 \rangle$ screw dislocation at high strain rate)	T (generated by $1/2 \langle 1\,1\,1 \rangle$ screw dislocation at high strain rate)	$(1/2 \langle 1\,1\,1 \rangle$ screw dislocations glide in {1 1 0} planes due to anti-twinning)	$(1/2 \langle 1\,1\,1 \rangle$ screw dislocations glide in {1 1 0} planes due to anti-twinning) + (axial symmetry of stress field)
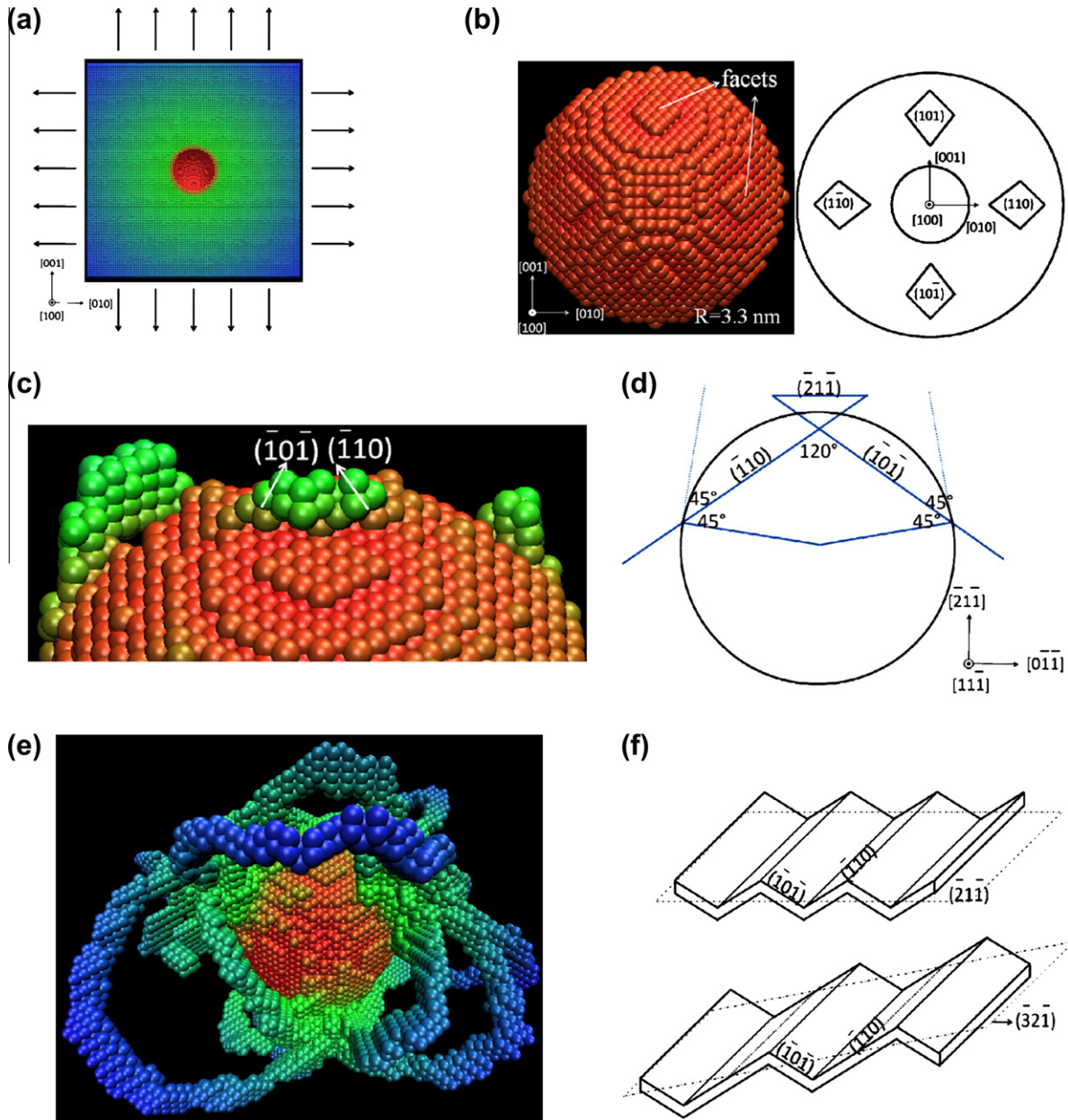
Fig. 4. Dislocation loop nucleation in hydrostatic tension at strain rate of $10^8\,s^{-1}$ ($R = 3.3$ nm). (a) Cross-section of a sample with a void at the center. (b) Initial faceted void surface. (c) Nucleation of a {1 1 2} shear loop by two {1 1 0} stacking faults intersecting the void surface at 45°. (d) Schematic showing the traces of two {1 1 0} slip planes intersecting a void at 45° to its surface. (e) Well-formed shear loop comprising two {1 1 0} components. The color scale here and in subsequent similar figures indicates radial distance from the center of the void, with the void surface in red and atoms farther away in blue. For defect visualization, only non-bcc atoms are shown. (f) Schematic showing a {1 1 2} plane and a {1 2 3} plane formed by two {1 1 0} planes (non-planar). In uniaxial tension, there is also only one shear loop along each ⟨1 1 1⟩ direction, lying on formed by two {1 1 0} planes. (For interpretation of the references to color in this figure legend, the reader is referred to the web version of this article.)

due to their lower mobility. They align along ⟨1 1 1⟩ directions in the {1 1 0} planes. Along each ⟨1 1 1⟩ direction there is only one shear loop lying on two {1 1 0} planes (non-planar). In uniaxial tension, there is also only one shear loop along each ⟨111⟩ direction, lying on a {1 1 2} plane. This is consistent with a Schmid factor analysis. The three slip planes sharing the common direction [1 1 1] are (1$\bar{2}$1), (11$\bar{2}$), and ($\bar{2}$1 1). The Schmid factors are:

$(1\bar{2}1)[1\,1\,1]: \quad m = 0.235$

$(1\,1\bar{2})[1\,1\,1]: \quad m = 0.235$

$(\bar{2}1\,1)[1\,1\,1]: \quad m = 0.471$

Thus, the ($\bar{2}$1 1) [1 1 1] system is activated first. This is shown schematically in the sequence shown in Fig. 6, where the three planes sharing the same [1 1 1] direction are shown, and a dislocation loop forming in the ($\bar{2}$1 1) plane is also shown. It should be noted that the extremities of these dislocation loops have to remain attached to the void surface for matter transport to occur. This important aspect has been discussed by Bulatov et al. [24] and Bringa
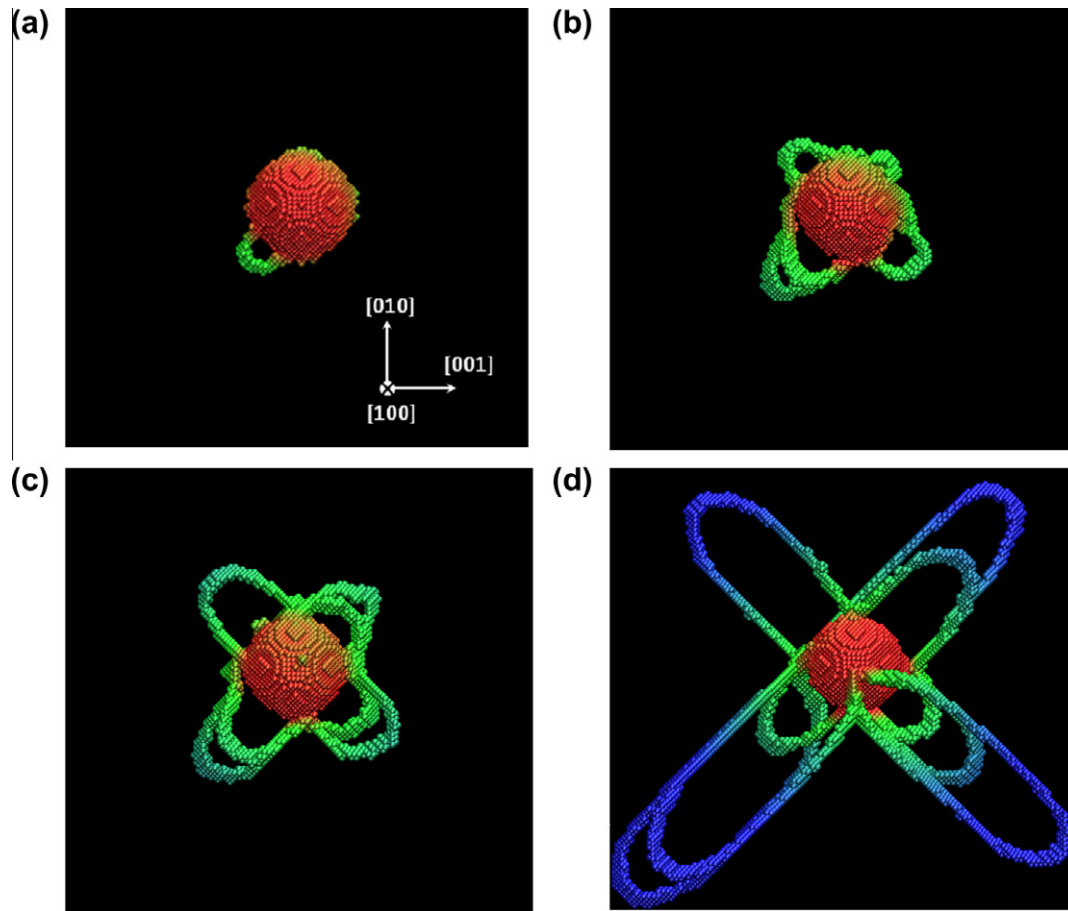
Fig. 5. Sequence of shear-loop formation in uniaxial compressive strain at a strain rate of 10^8 s^{-1} ($R = 3.3$ nm). These are referred to as "dislocation loops" by Marian et al. [30] in his static QC simulations.
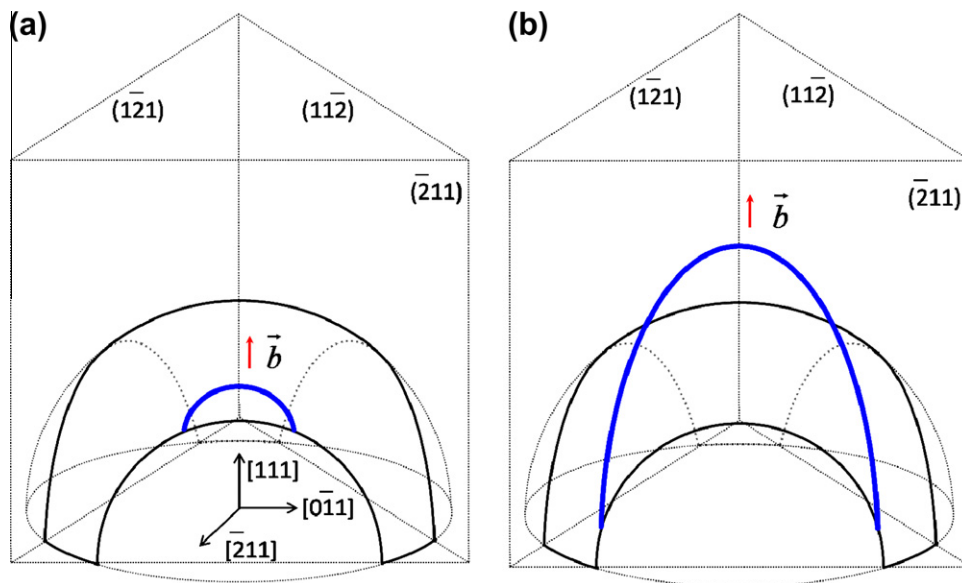

Fig. 6. Schematic showing formation of a shear loop in uniaxial tensile strain.

et al. [25]. In this sense, the dislocation loops are different from conventional shear loops. If one considers the tridimensional aspects, one has more than one slip system with the highest Schmid factor. This is clear from the simulation in Fig. 5 and from Fig. 7, which shows four slip planes of the {1 1 2} family, each contributing one loop.
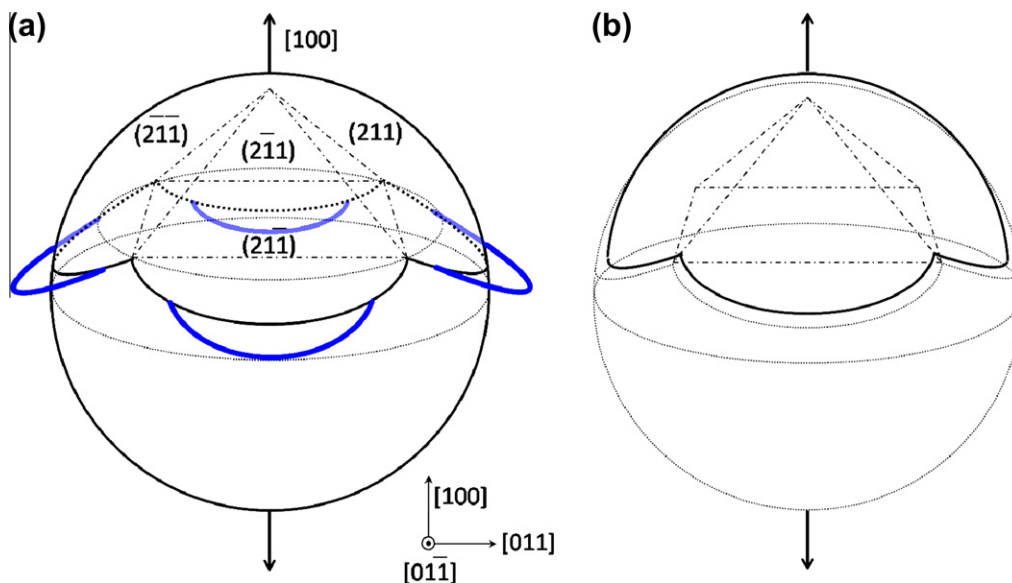
Fig. 7. Schematic showing formation of shear loops on four {1 1 2} planes with expansion of the void under uniaxial tensile strain.

The cooperative expansion of the loops produces the growth of the void.

Nucleation of shear loops under hydrostatic tensile and compressive strain is similar to that under uniaxial tensile and compressive strain. Sequence of defect evolution in hydrostatic tensile strain at a strain rate of $10^8 \, s^{-1}$ is shown in Fig. 8. One important difference is that loops are simultaneously generated on a greater number of slip systems, by virtue of the fact that the Schmid factors for all systems are identical. This can be seen by comparing Figs. 5a and 8a. In hydrostatic tension, along each ⟨1 1 1⟩ direction there are three shear loops lying on the three {1 1 2} planes parallel to the same ⟨1 1 1⟩ direction.

4.3. Formation of prismatic loops

In hydrostatic tension, due to the spherical symmetry of stress field, all 12 of the {1 1 2} slip planes have the same resolved shear stress. As a consequence, along each ⟨1 1 1⟩ slip direction, there are three shear loops lying on the three {1 1 2} slip planes that are parallel to the same ⟨1 1 1⟩ direction. Fig. 9 shows the evolution of defects in this configuration. The total possible number of shear loops is 24, although some of them develop at a slower rate. As the shear loops expand in {1 1 2} planes, three loops lying in the three {1 1 2} planes that parallel to the same ⟨1 1 1⟩ direction can meet and react. The screw components of these three loops have the same Burgers vector $\mathbf{b} = 1/2 \, \langle 1 \, 1 \, 1 \rangle$ but the dislocation line directions are opposite, so they cancel each other, only leaving the edge components. These detached edge dislocations are connected with each other and form a triangular dislocation loop, namely a prismatic loop, as shown in Fig. 9c and d. After the cancellation of screw dislocations, new shear loops are generated from the void surface, as shown in Fig. 9d, and the prismatic loop emission starts again. This prismatic

loop formation by three shear loops interacting is schematically shown in Fig. 10. In Fig. 10b, three loops are emitted, on (1 2̄ 1), (2̄ 1 1) and (1 1 2̄), which have a common intersection [1 1 1]. The screw components of the shear loops cancel each other ($\overrightarrow{b_1} + (-\overrightarrow{b_3})$; $\overrightarrow{b_3} + (-\overrightarrow{b_2})$; $\overrightarrow{b_2} + (-\overrightarrow{b_1})$), and the edge components form a triangular loop. As the triangular loop moves outward, the volume of the void is enlarged by the displacement between lattices inside and outside the triangular prism, as shown in Fig. 10d.

In hydrostatic compression, the situation is similar but the shape of the prismatic loops generated is hexagonal, not triangular. This is shown in Fig. 11. After the nucleation of two {1 1 0} faults intersecting the void surface at 45°, subsequent slip occurs still in the same {1 1 0} planes, not alternately in two {1 1 0} planes, as shown in Fig. 12a. This will not form a {1 1 2} fault. After the dislocation reaction, nonplanar shear loops lying on two {1 1 0} planes are formed. Also, along each ⟨1 1 1⟩ direction there are three non-planar shear loops lying on {1 1 0} planes parallel to the same ⟨1 1 1⟩ direction. Some of these loops are of smaller size. As slip occurs in {1 1 0} planes, these shear loops lying on {1 1 0} planes that parallel to the same ⟨1 1 1⟩ direction meet and react. Hexagonal prismatic loops are formed, as shown in Figs. 11d and 12b. This behavior was never seen in the MD simulations of Bringa et al. for fcc copper [23], because the formation of extended stacking faults and shear loop reactions did not allow for the formation of prismatic loops. However, a mechanism akin to the one presented by Bulatov et al. [24] and predicting rectangular loops is feasible.

4.4. Twinning

At the higher strain rate of $10^9 \, s^{-1}$ (in hydrostatic tension and under uniaxial tensile strain), two {1 1 0} stacking faults intersecting the void surface at 45° nucleate initially at the void surface. However, after their generation, twins

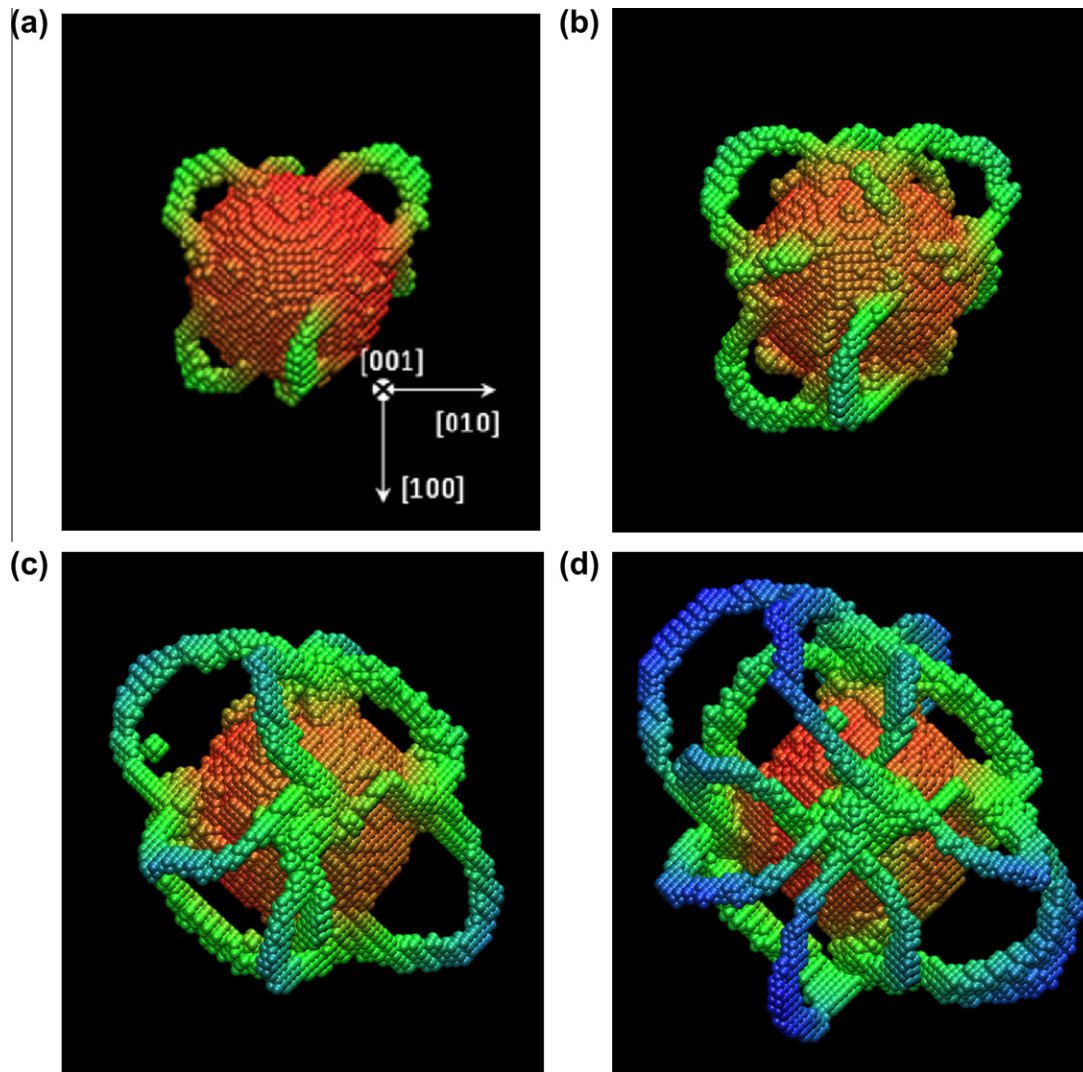Fig. 8. Propagation of multiple shear loops in hydrostatic tensile loading at a strain rate of 10^8 s^{-1} ($R = 3.3$ nm).

are formed on the {1 1 2} planes (these are the twinning planes in bcc lattice), representing the combination of these two {1 1 0} planes, as discussed in Section 4.1. Their expansion in uniaxial tension is shown in the MD sequence of Fig. 13. As the stress increases, these twin boundaries spread outwards in the {1 1 2} planes; atoms on those {1 1 2} planes adjacent to the formed {1 1 2} twin boundaries will glide along ⟨1 1 1⟩ directions sequentially, thickening these twins. As the twins grow, the volume of the void is enlarged by the cooperative shear displacement. Along each ⟨1 1 1⟩ slip direction, there is at most one twin lying on a {1 1 2} plane parallel to the ⟨1 1 1⟩ direction. Twinning in uniaxial tensile strain is schematically shown in Fig. 14. Only one twin is activated, in the system having the highest Schmid factor.

In hydrostatic tensile stress, due to the spherical symmetry of stress field, along each ⟨1 1 1⟩ slip direction, three twins lying on the three {1 1 2} planes parallel to the same ⟨1 1 1⟩ direction are formed. The MD simulation sequence is shown in Fig. 15, while Fig. 16 shows the schematic

evolution of three twin planes being simultaneously activated.

Interestingly, twins were only observed when the stress was tensile (uniaxial strain or hydrostatic stress). Section 4.5 provides a rationale for this stress dependence. Using the QC method, Marian et al. [30] observed twinning for uniaxial compression, but only when they maximized the twinning shear (loading along [4̄ 8 1 9]), identified the observed defects as twins on (1 1 0) planes. We observed similar features as the ones observed by Marian et al. [30] for strain rates of 10^{10} s^{-1} (Fig. 17). However, in our case, these features can be identified as partial dislocations on {1 1 0} planes with a Burgers vector along [1 1 1]. Twinning in our simulations might be related to the twinning process observed by Marian et al. [61].

4.5. Constitutive description of the slip-to-twinning transition

To estimate the slip-to-twinning transition at high strain rate and under shock compression, Meyers et al. [62]
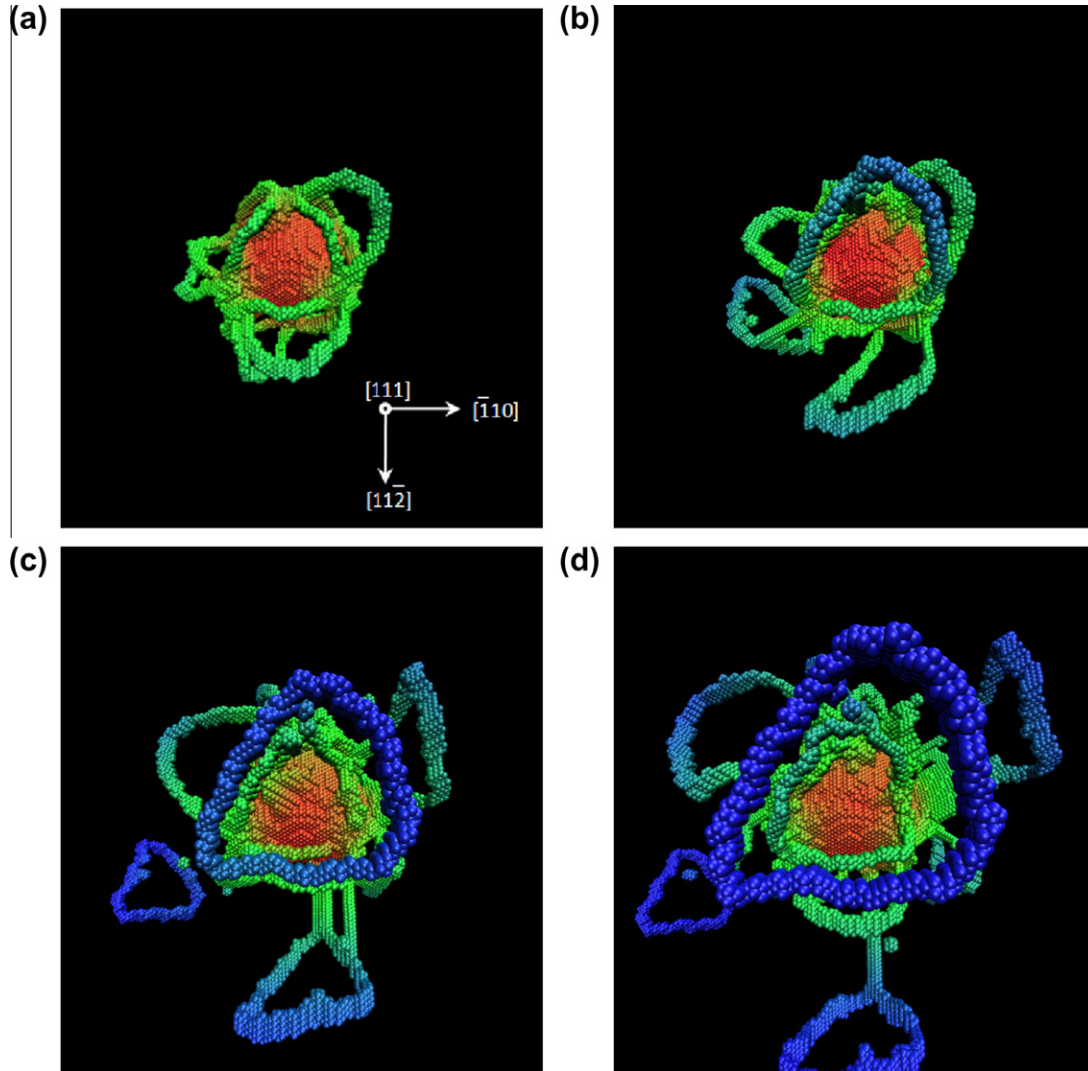
Fig. 9. Sequence showing formation of shear loops and triangular prismatic loops in hydrostatic tensile loading at a strain rate of 10^8 s^{-1} ($R = 3.3$ nm).

developed an analysis that has been successfully applied to copper [63] and nickel [64]. It is based on the simple premise that slip and twinning are competing mechanisms, and that the one requiring the lowest applied shear stress operates. Here this analysis is extended to a bcc metal, tantalum. The yield stress induced by slip can be expressed by the Zerilli–Armstrong equation [65] for bcc metals:

$$\sigma_S = \text{athermal stress} + C_2 e^{-C_3 T} \dot{\varepsilon}^{C_4 T}$$
$$= \sigma_S^* + C_2 e^{-C_3 T} \dot{\varepsilon}^{C_4 T} + k_S d^{-1/2} \quad (5)$$

where C_2, C_3, C_4 and k_s are parameters for tantalum, σ_S^* is the athermal stress (not including the grain-size effect), $\dot{\varepsilon}$ is the strain rate, T is the temperature and d is the grain size. The values of these parameters C_2, C_3 and C_4 have been established by Zerilli and Armstrong [66] for polycrystalline tantalum based on experimental results by Hoge and Mukherjee [67] at low strain rates. The following values were used [66]: $C_2 = 1125$ MPa, $C_3 = 0.00535$ K^{-1}, $C_4 = 0.00024$ K^{-1}. The value of C_4 was changed from its original value of 0.000327 K^{-1} to 0.00024 K^{-1} to fit the

results of Rittel et al. [68] at both low and high strain rates (solid circles and dash line in Fig. 18), and details are given in a separate paper discussing experimental results [69]. Sherwood et al. [70] observed slip and twinning in both tension and compression of [1 0 0] monocrystals, therefore their experimental results are used in this analysis. The value of $\sigma_S^* + k_S d^{-1/2}$ for slip was obtained by translating the experimental values by Rittel et al. [68] down to accommodate the results of experimental yield stress for monocrystalline tantalum along [1 0 0] by Sherwood et al. [70] (solid triangle in Fig. 18): $\sigma_S^* + k_S d^{-1/2} = -26.4$ MPa. It should be noted that the yield stresses in tension and compression are almost the same at room temperature [70]. Thus, the asymmetry of yield stress due to dislocation core effects [31–35,71], which is significant at lower temperatures, is non-existent at 300 K for tantalum. In contrast, there is a significant difference for tungsten and molybdenum [71] at 300 K.

The effect of strain rate on twinning can be neglected, to a first approximation. We are also neglecting the effect of temperature on twinning, since the temperature rise due
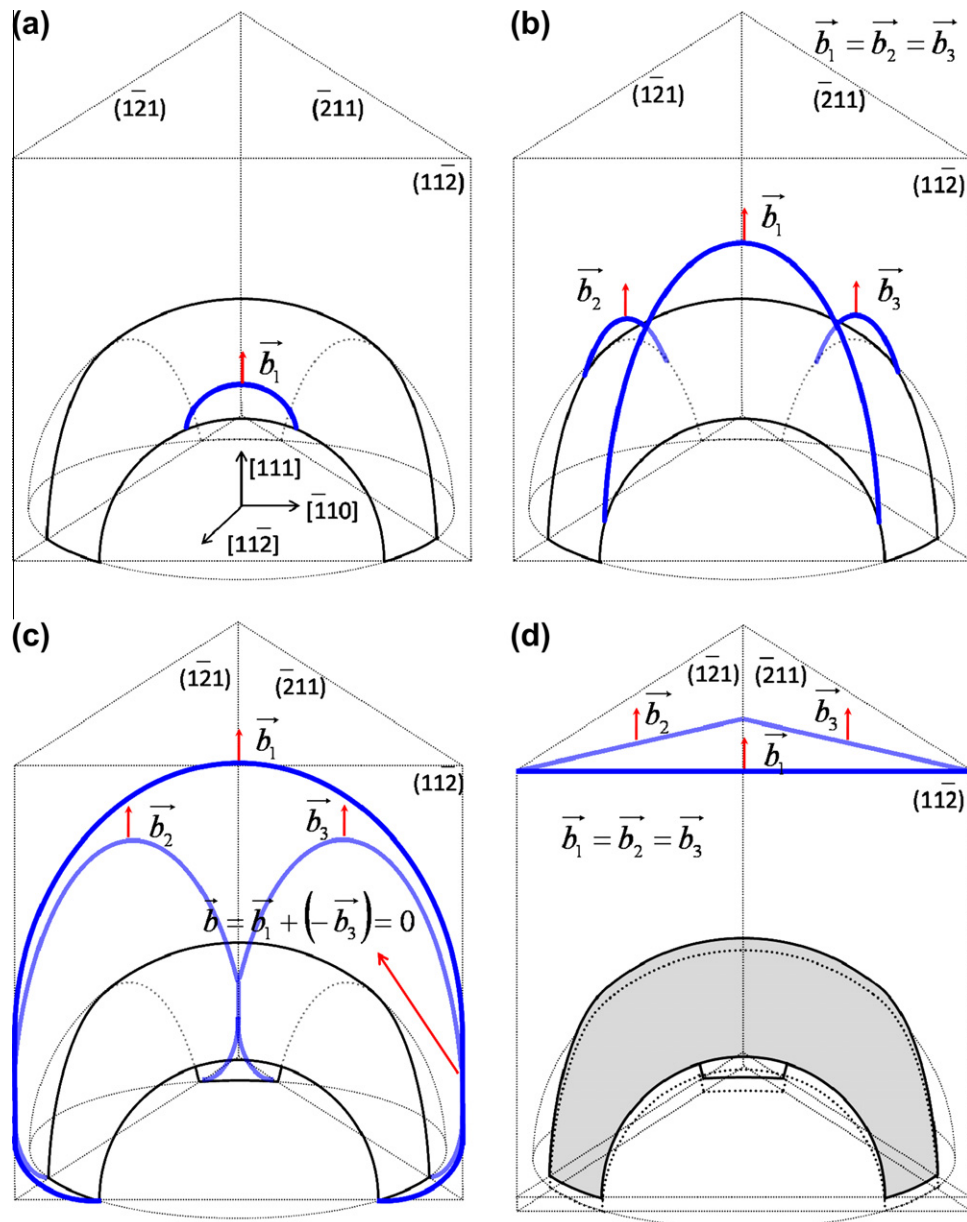
Fig. 10. Emission of shear loops leading to prismatic loop formation in hydrostatic tension. (a and b) Shear loop emission on three {112} planes (($1\bar{2}1$), ($\bar{2}11$) and ($11\bar{2}$)) which share a common direction [1 1 1]; (c and d) formation of a triangular prismatic loops.

to plastic activity in our simulations was relatively small. The twinning stresses established by Sherwood et al. [70] in tension and compression for loading along [1 0 0] were 378 and 771 MPa, respectively. Thus, the twinning stress in tension is half of the one in compression. The slip-to-twinning transition strain rates in tension and compression can be predicted, as shown in Fig. 18. The predicted transition strain rates in compression (1×10^7 s^{-1}) is in qualitative agreement with experimental values [69], although the predicted transition strain rate in tension (4×10^2 s^{-1}) is much lower than the simulation result (10^8–10^9 s^{-1}). Considering the many simplifications in the current analysis, the results are in qualitative agreement with the analysis above. The values for the twinning threshold used above correspond to experimental values for macroscopic Ta

crystals, which are likely to have abundant dislocation sources. On the other hand, our calculations use single crystals with approximate size 33 nm that are devoid of dislocations or other defects except for the initial void. Thus, their strength level is much higher than the experimentally observed values. This is a well-known effect at the nanoscale, where single crystals and even polycrystals show tremendous strength for both fcc and bcc materials [72].

4.6. Experimentally observed defects

Although the MD simulations did not produce twinning under compression of the voids, it can occur experimentally if sufficiently high shear stresses are reached, as demonstrated by shock compression experiments on Ta crystals
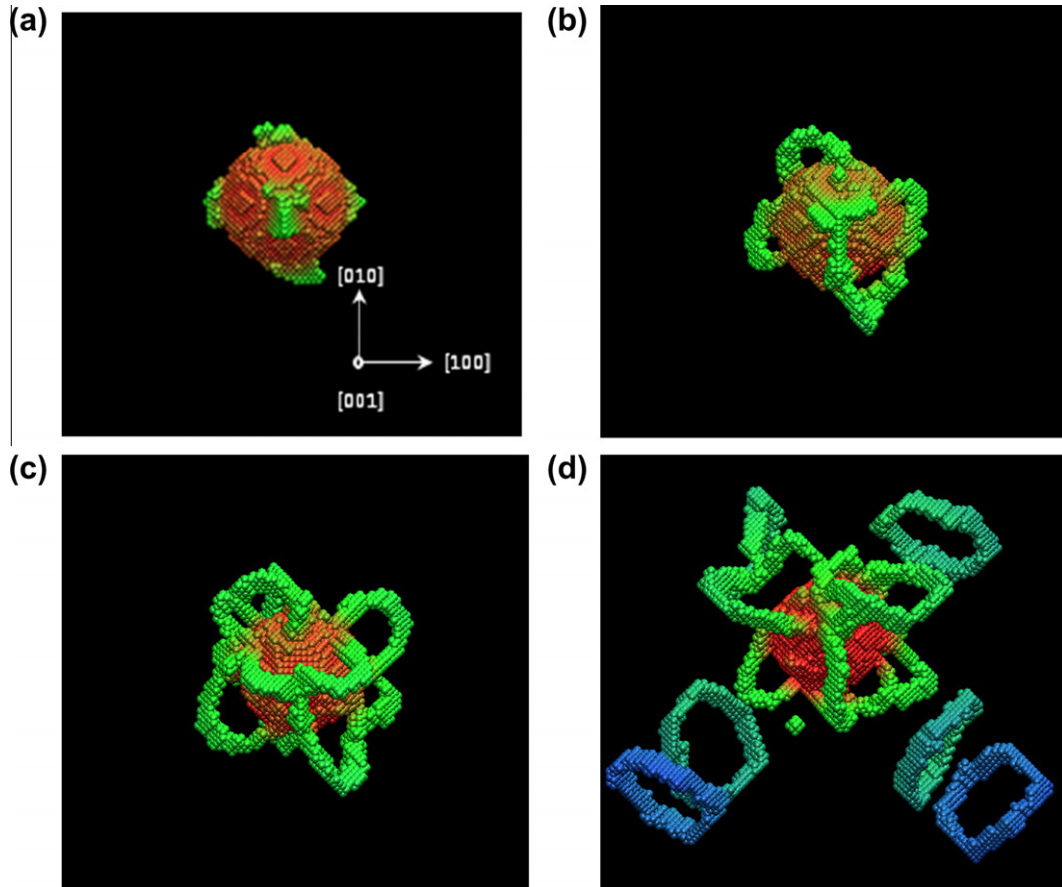
Fig. 11. Sequence of shear loop emission leading to hexagonal prismatic loops formation and detachment in hydrostatic compression at a strain rate of 10^8 s^{-1} ($R = 3.3$ nm).
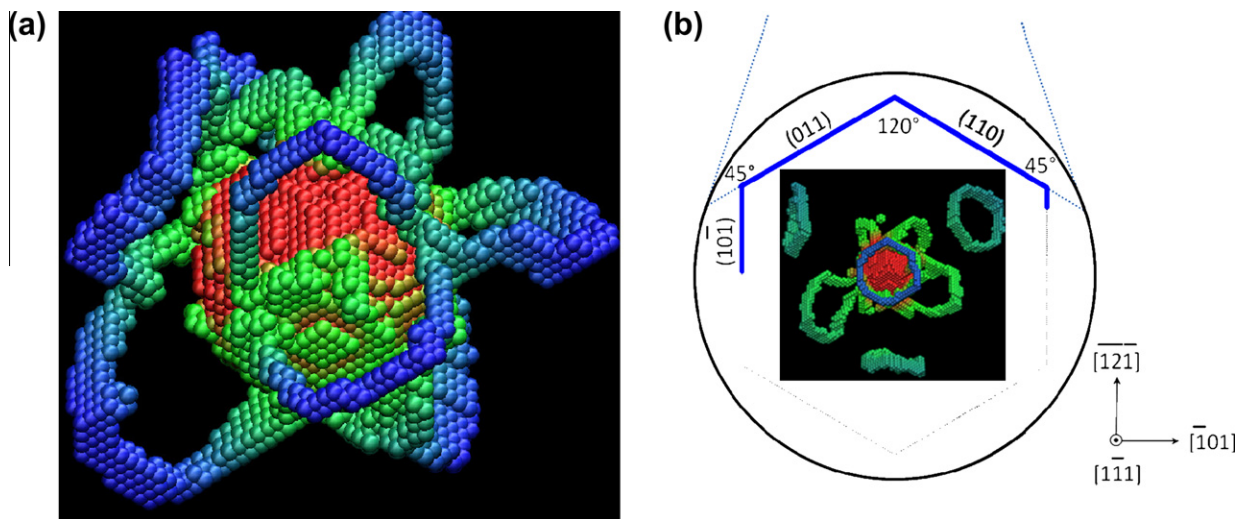

Fig. 12. Screw components of shear loops gliding in {1 1 0} planes in hydrostatic compression at 10^8 s^{-1} ($R = 3.3$ nm). The inset in (b) shows hexagonal loops formed by shear loops.

in gas guns [65,73] and lasers [69] in which stresses as high as 100 GPa can be reached.

Experiments conducted using laser energy to generate shock pulses [69] confirm the slip-to-twinning transition in compression when the pressure exceeds ~35 GPa. These laser compression experiments were carried out using high-energy Nd-glass pulsed laser beams with a face plate and generated strain rates on the order of 10^8–10^9 s^{-1} for times on the order of nanoseconds. This extreme regime is the closest possible to MD simulations, in which strain rates

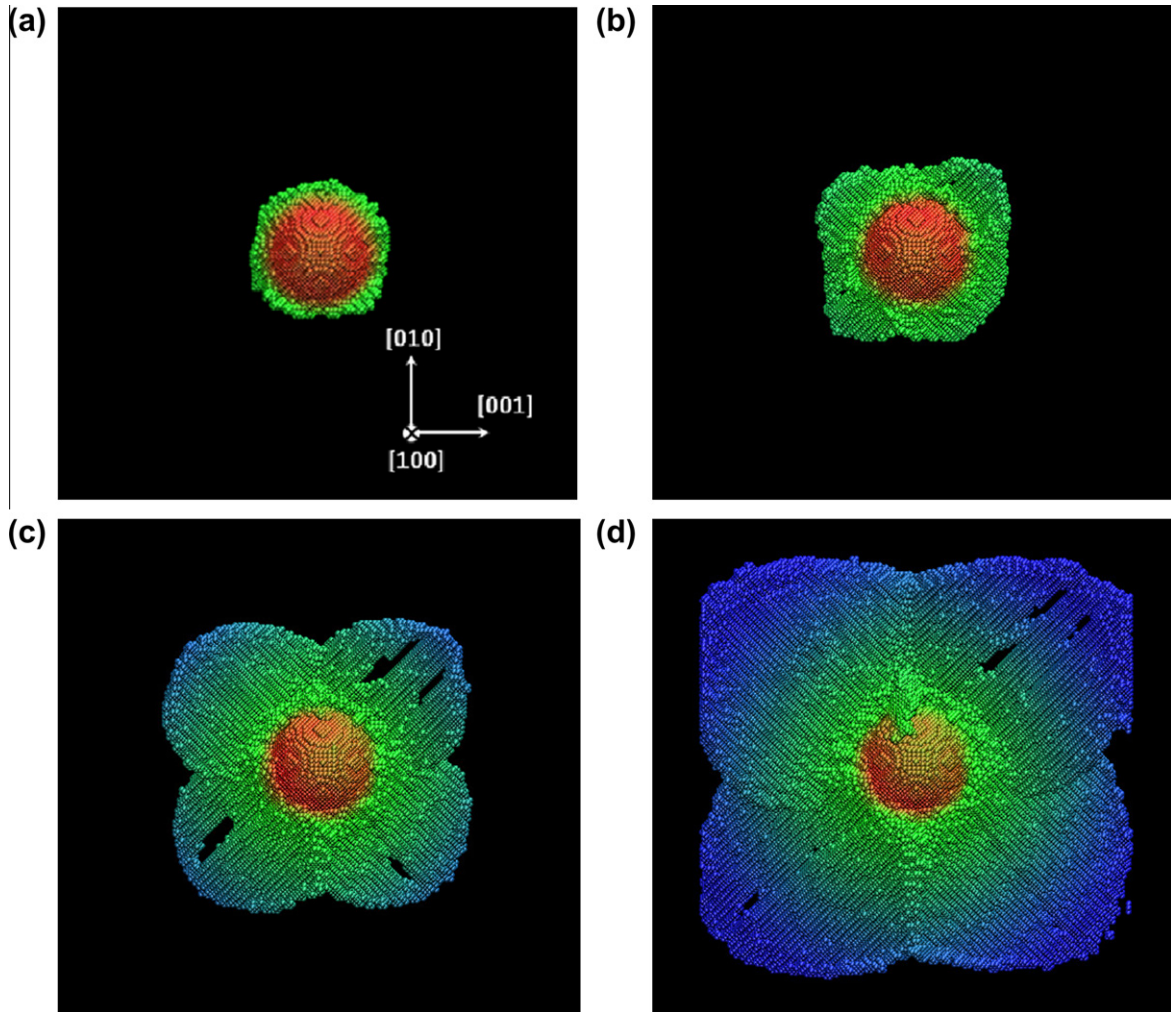Fig. 13. Sequence of defect evolution (formation of {1 1 2} twins) in uniaxial tensile strain at a strain rate of 10^9 s^{-1} ($R = 3.3$ nm).
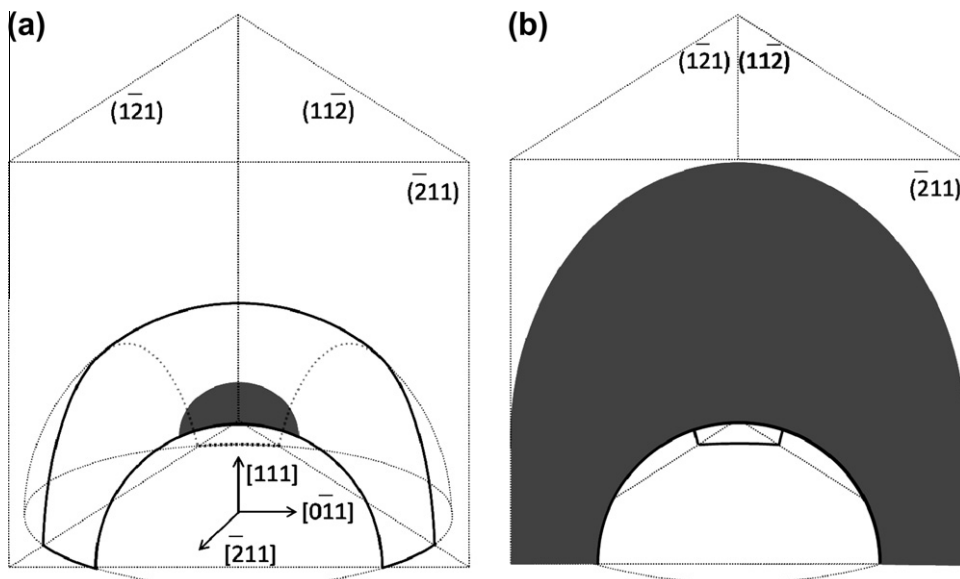

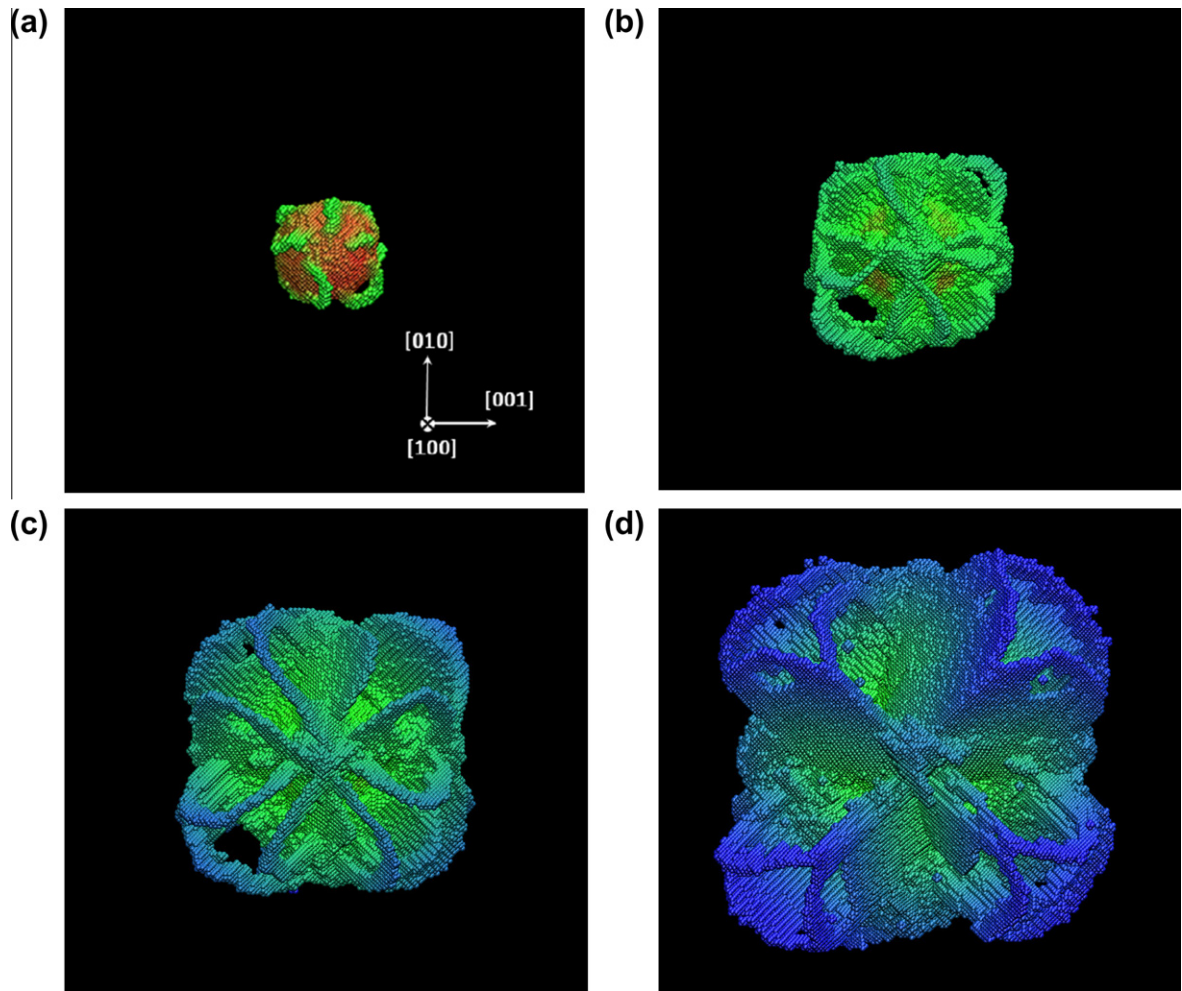Fig. 14. Schematic showing twinning in uniaxial tensile strain at strain rate of 10^9 s^{-1}; only one plane is activated.

Fig. 15. Sequence of defect evolution (twins, and also some dislocation loops) in hydrostatic tensile loading at a strain rate of 10^9 s^{-1} ($R = 3.3$ nm).
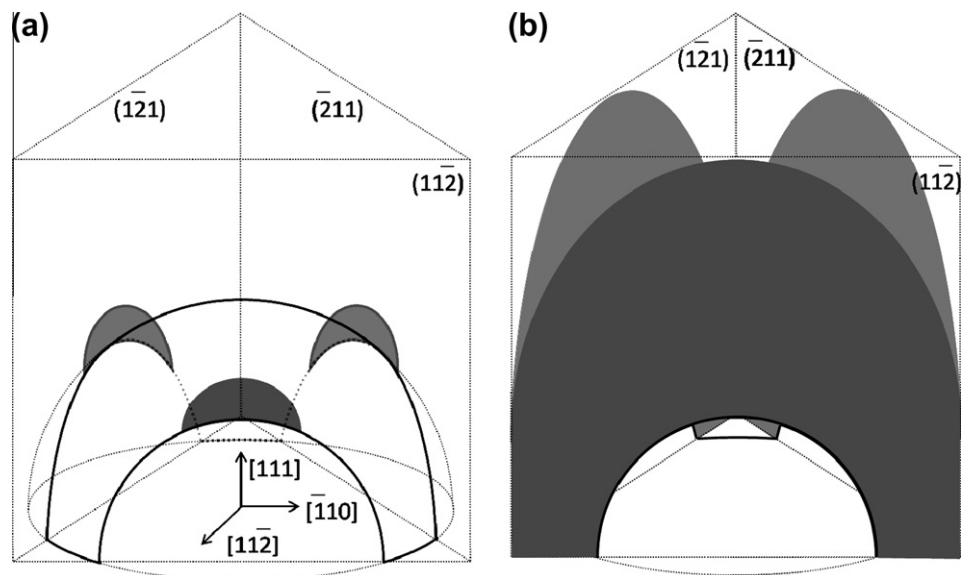

Fig. 16. Schematic showing twinning under hydrostatic tensile loading; three planes are simultaneously activated.

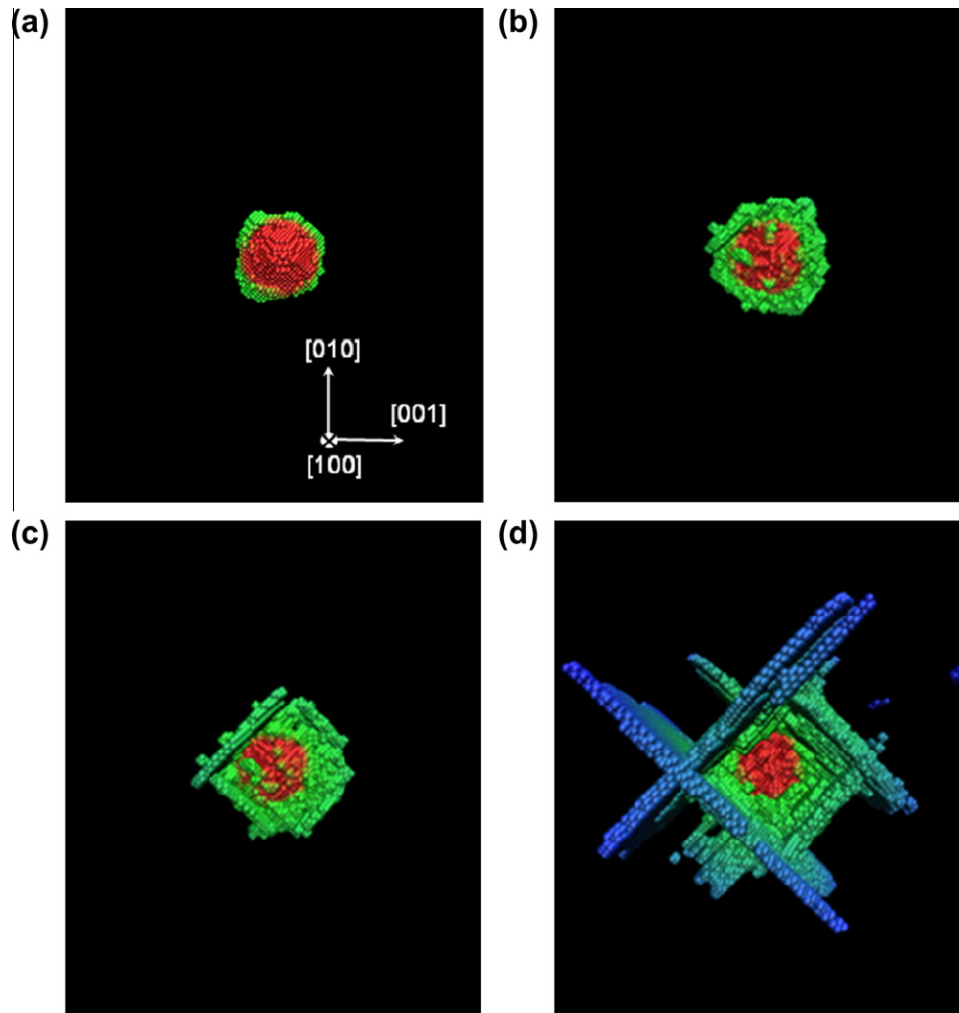Fig. 17. Sequence of defect evolution under uniaxial compressive strain along [1 0 0] at a strain rate of 10^{10} s^{-1} ($R = 2$ nm). Planar defects are lying on two {1 1 0} planes with zero Schmid factor, namely (0 1 1) and (0 1 $\bar{1}$), forming a rectangle surrounding the void.
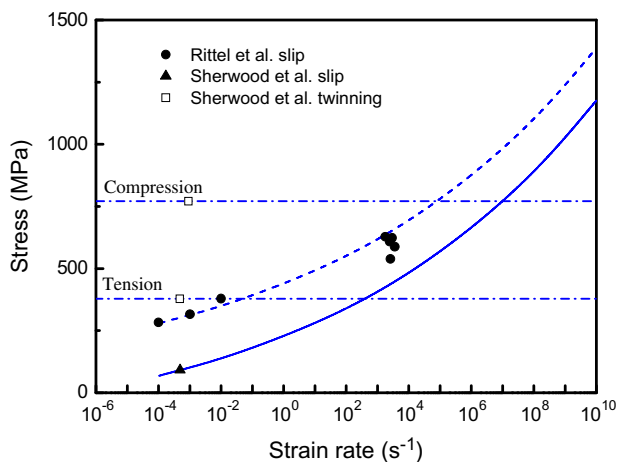

Fig. 18. Slip/twinning stress as a function of strain rate. Slip-to-twinning transition occurs at the intersection of slip stress and twinning stress. Twinning stress is fitted to experimental values and is therefore significantly lower than values resulting from atomistic simulations.

usually vary from 10^7 to 10^{10} s^{-1} and loading times are on the order of picoseconds.

The characteristic deformation structures observed in a [1 0 0] Ta monocrystal loaded in uniaxial strain are illustrated in Fig. 19. Fig. 19a shows dislocations generated at a compressive stress of ∼20 GPa; this is a comparable value to the stress in Fig. 5, which is ∼15 GPa, also in uniaxial compressive strain. In the actual shock compression experiments the dislocations are not nucleated at voids but are the result of the existing (pre-shock) dislocation structure. Fig. 19b shows twinning in the same [1 0 0] monocrystal shock compressed to a stress higher than 35 GPa. The twins form on {1 1 2} planes and have thicknesses of ∼0.2 μm. These twins have dimensions much higher than the ones in the current MD simulations because of the differences in the two regimes, including sample size (3 mm vs. 33 nm), loading time (3 ∼ 10 ns in laser shock compression vs. ∼10 ps in MD) and stress level. These observations illustrate the nature of the deformation processes.

4.7. Analysis of generalized stacking fault energies

The generalized stacking fault energies γ (**f**) for {1 1 0}, {1 1 2} and {1 2 3} slip planes gliding along ⟨1 1 1⟩
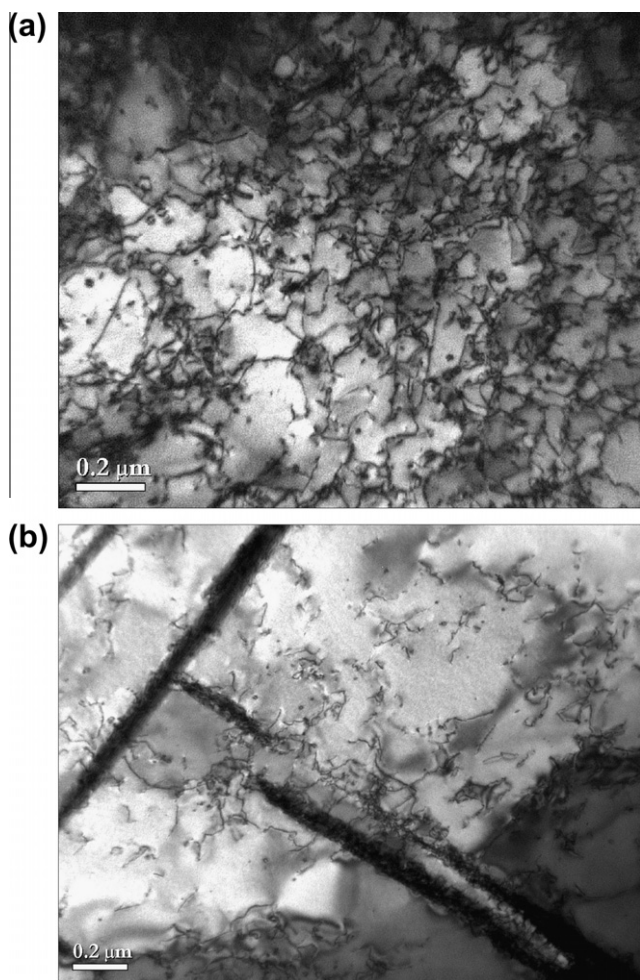
Fig. 19. TEM micrographs of (a) dislocations and (b) mechanical twinning in laser shocked [1 0 0] Ta monocrystal at a strain rate of $10^9 \, s^{-1}$, energy level of 684 J, pulse duration of ~10 ns and input energy of ~600 J mm^{-2}.

Fig. 20. Generalized stacking fault energies γ (f) for slip along $\langle 1\,1\,1 \rangle$ directions in $\{1\,1\,0\}$, $\{1\,1\,2\}$ and $\{1\,2\,3\}$ slip planes. f is the displacement vector, $f = |\mathbf{f}|$, $b = |1/2 \langle 1\,1\,1 \rangle|$. Relevant displacements are noted. Values of the maximum generalized stacking fault energies calculated by others [74–76] are also included.

directions are shown in Fig. 20, where $\mathbf{f}$ is the displacement vector, f is the magnitude of $\mathbf{f}$ and the magnitude of the Burgers vector $\mathbf{b}$ is $b = |1/2 \langle 1\,1\,1 \rangle|$. Generalized stacking fault energies for slip planes gliding along other directions were not calculated because the principal slip directions in bcc lattice are $\langle 111 \rangle$. Values of the maximum generalized stacking fault energies calculated by others [74–76] using different methods, such as the first-principles-based force fields method (qEAM) [74], the angular-dependent potential (ADP) [75], ab initio calculations [75] and the model generalized pseudopotential theory (MGPT) [76], are also included in Fig. 20 for comparison. The fact that the current results agree well with different simulations validates the use of this extended Finnis–Sinclair potential for plasticity studies.

All stacking faults in $\{1\,1\,0\}$, $\{1\,1\,2\}$ and $\{1\,2\,3\}$ slip planes with the fault vector in $\langle 1\,1\,1 \rangle$ directions are unstable (there is no minimum energy point), as shown in Fig. 20. This is different from stacking faults in fcc lattice [77]. The curve of $\gamma (f) \sim f$ for $\{1\,1\,0\}$ planes is symmetric
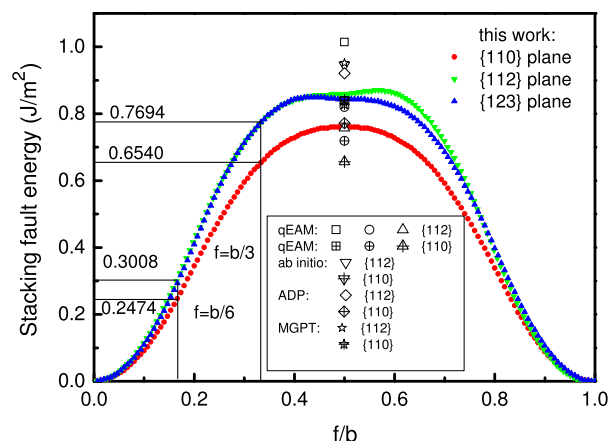
with respect to $f = b/2$, which means that gliding along the opposite direction $[\bar{1}\,\bar{1}\,\bar{1}]$ is equivalent to gliding along $[1\,1\,1]$. On the other hand, curves for $\{1\,1\,2\}$ and $\{1\,2\,3\}$ planes are asymmetric. For $\{1\,1\,2\}$ planes the energy curve is smoother when gliding in the $[1\,1\,1]$ direction than in the opposite direction; this is well known as twinning and anti-twinning asymmetry [31], although the amount of asymmetry is small, as observed in ab initio calculations [75]. It is also worth noting that, among these three slip planes, $\{1\,1\,0\}$ planes have the lowest stacking fault energies for all values of f, which accounts for the nucleation of stacking faults in $\{1\,1\,0\}$ planes, as shown in Fig. 4c. Energies for $\{1\,1\,2\}$ and $\{1\,2\,3\}$ plane faults have almost the same values except for the region near the maximum point, but are higher than energies for $\{1\,1\,0\}$ fault. For each of the $\{1\,1\,0\}$, $\{1\,1\,2\}$ and $\{1\,2\,3\}$ plane faults, the energy for $f = b/3$ is higher than twice of that for $f = b/6$, namely $\gamma (b/3) > 2\gamma(b/6)$, which means that an $f = b/6$ fault is preferable to an $f = b/3$ fault. Calculations for samples initially at finite stress and temperature might also contribute to the understanding of defect generation under extreme conditions.

4.8. Analysis of stress–strain response and dislocation velocity

The stress–strain curves of samples with 3.3 nm voids in uniaxial strain and hydrostatic stress are shown in Fig. 21a and b, respectively. In Fig. 21, the strains at which defects start to nucleate are indicated by arrows. In all cases, the yield stresses increase with the increasing strain rate. In uniaxial tensile strain and hydrostatic tension, the stress–strain curves drop precipitously, due to the stress release by the expanding void, while there are no obvious stress drops in the stress–strain curves in uniaxial compressive strain and hydrostatic compression. These stress levels are, as commented earlier, much higher than the

Fig. 22. Position of dislocations emanating from collapsing void ($R = 3.3$ nm, uniaxial compressive strain) in tantalum (bcc) specimens vs. time. The slope of linear fits to the MD results gives the dislocation velocity. For reference, the transverse sound velocity along the [1 0 0] direction $(G/\rho)^{1/2}$ for Ta is $\sim 2 \times 10^3$ m s^{-1} [55].

A dislocation velocity vs. stress relation for tantalum was also calculated by Deo et al. [78] using a stochastic method. Their applied stress σ^A was normalized by the Peierls stress τ_p. For comparison we also normalized the applied stress by the Peierls stress. Since there is no available Peierls stress τ_p calculated using the extended Finnis–Sinclair potential, we use instead the relation $\tau_p = 0.043\, C_{44}$ calculated using the Finnis–Sinclair potential [29] by Gröger and Vitek [34]. The shear modulus C_{44} is 87.4 GPa using the extended Finnis–Sinclair potential [55], and thus $\tau_p = 3.76$ GPa. The calculated dislocation velocities v_D as a function of normalized stresses σ^A/τ_p are shown in Fig. 23. Deo et al.'s [78] results (only for $T = 300$ K) are also included in Fig. 23. It can be seen from Fig. 23 that there is a good agreement between our results and the linear extrapolation of Deo et al.'s [78] results. We note, however, that dislocation mobility in bcc metals is extremely complex, as shown by Jin et al. [79] and Marian
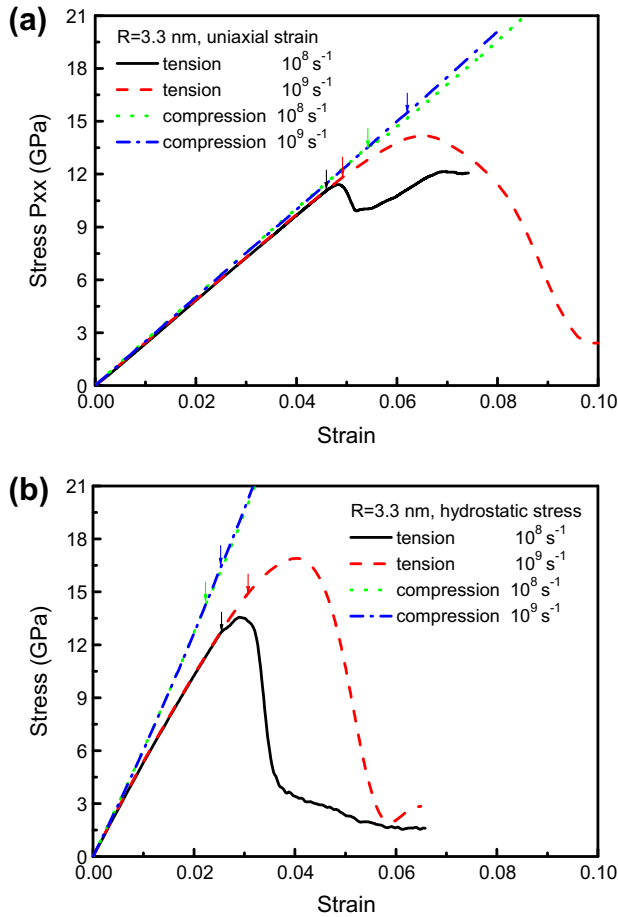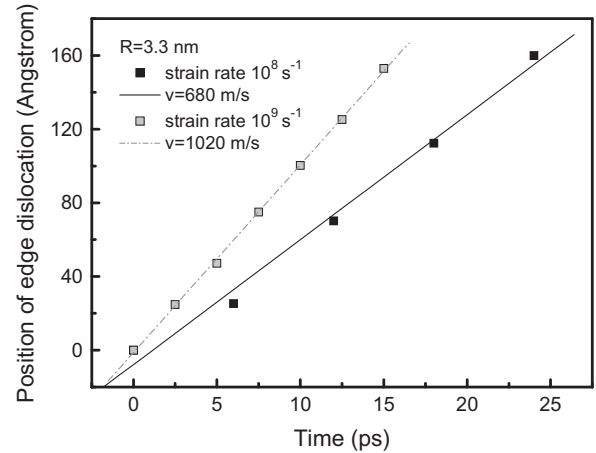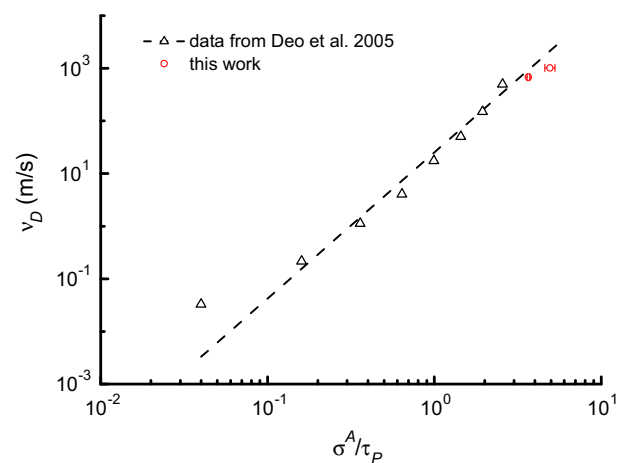

Fig. 21. Stress–strain curves for void growth and collapse in uniaxial strain (a); and hydrostatic stress (b). Yield strains at which defects start to nucleate are indicated by arrows. For compression, the negative stresses and strains curves are plotted.

experimental values used in Section 4.5 and this is one of the reason for the differences observed.

Dislocation velocities can also be obtained in our MD simulations, in a manner similar to that shown for fcc crystals by Dávila et al. [21] and Bringa et al. [23]. For copper, they obtained both subsonic and transonic dislocations, depending on the applied stress level. The transonic dislocations are from molecular dynamics simulations by Dávila et al. [21] of copper under shock compression; this suggests the existence of partial dislocation loops expanding at velocities exceeding the shear wave speed. At the higher stresses (21 GPa) the velocity of the partial loops (4.4 km s^{-1}) was higher that the bulk sound velocity (4 km s^{-1}). In our simulations, dislocation velocities in uniaxial compressive strain for tantalum are also calculated by tracking the dislocation front as a function of time, as shown in Fig. 22. Dislocation velocities in uniaxial compressive strain at strain rates of 10^8 and 10^9 s^{-1} are 680 and 1020 m s^{-1} respectively, which are subsonic. The stress levels corresponding to the dislocation motion in uniaxial compressive strain can be obtained from Fig. 21a, and are about 13.5–14.0 and 17.3–19.8 GPa at the strain rates of 10^8 and 10^9 s^{-1}, respectively.

Fig. 23. A log–log plot of the dislocation velocity v_D as a function of the normalized stress σ^A/τ_ρ.

et al. [61]. For instance, Marian et al. [61] found that at high strain rates screw dislocation motion in Fe leads to the production of defect debris and eventually to twinning. The points presented here are in the same regime that Marian et al. [61] saw roughening during screw dislocation motion; however, edge dislocations would behave differently. We should point out that Gumbsch and Gao [80] have reported supersonic dislocations in tungsten (also bcc) from simulation.

5. Conclusions

1. Three deformation mechanisms in void growth and collapse are identified and evaluated: (i) shear loop emission and subsequent expansion from the surface of the void; (ii) cooperative shear loop emission from slip planes which are parallel to the same $\langle 1\,1\,1 \rangle$ slip direction, and their combination forming prismatic loops; and (iii) twinning starting at the void surface. The shapes of the formed prismatic loops are different in hydrostatic tension and compression, triangular in tension and hexagonal in compression.
2. The effects of stress states on deformation mechanisms are discussed: the number of activated slip systems is determined by the stress state. In hydrostatic stress, there are 24 activated slip systems, three along each $\langle 1\,1\,1 \rangle$ slip direction, which allows for the formation of prismatic loops. For uniaxial strain along [1 0 0], there are only eight activated slip systems, only one along each $\langle 1\,1\,1 \rangle$ slip direction, and prismatic loops are not able to be formed; the slip planes of screw components of formed shear loops are determined by the directions of loading (tension/compression asymmetry). In tension, screw components prefer to glide in $\{1\,1\,2\}$ planes, since these $\{1\,1\,2\}$ planes are twinning planes. In compression, screw components prefer to glide in $\{1\,1\,0\}$ planes, since now $\{1\,1\,2\}$ planes are anti-twinning planes.
3. Effects of strain rate on deformation mechanisms are discussed: there is an obvious slip-to-twinning transition in tension (hydrostatic tension and uniaxial tensile strain) when the strain rate increases from 10^8 to $10^9\,\mathrm{s}^{-1}$. This transition appears because $1/2\,\langle 1\,1\,1 \rangle$ screw dislocations prefer to generate $\{1\,1\,2\}$ twins than glide at high strain rate; there is no significant strain-rate effect in compression (hydrostatic compression and uniaxial compressive strain), because screw dislocations prefer to glide in $\{1\,1\,0\}$ planes in compression and this glide seems not to be sensitive to strain rates up to $10^9\,\mathrm{s}^{-1}$. This slip-to-twinning transition is also observed in independent laser compression experiments and occurs at a pressure of approximately 35 GPa.
4. Analysis of the MD simulations predicts a slip-to-twinning transition strain rate in qualitative agreement with experiments and with a transition model fit to experimental results, but at a much higher strain rate. It should be emphasized that there are large differences between the experimentally obtained and computed twinning and slip stresses. The MD simulations apply to a single crystal with small dimensions (nanometers) that is devoid of pre-existing dislocations or other defects, except for the void. In contrast, the monocrystals tested experimentally have lateral dimensions of millimeters and contain defects. Nevertheless, a trend can be extracted from the results: the transition (from slip-to-twinning) strain rate in tension is much lower than in compression. This explains the formation of twins in tension and their absence in compression.
5. Laser compression experiments on tantalum monocrystals with the same [1 0 0] orientation produce dislocation networks at compressive stresses below 35 GPa and twins at stresses higher than this threshold. It is important to point out that twinning was observed in compression because in the shock loading experiments [65,69,73] stresses considerably higher than the MD stresses ($\sim$15 GPa) were reached.
6. Dislocation velocities are measured by tracking the far side of the edge components of the dislocation loop and are found to be $\sim$680 and $\sim$1020 m s^{-1} for imposed strain rates of 10^8 and $10^9\,\mathrm{s}^{-1}$ in uniaxial compressive strain, respectively. Our results are in good agreement with calculations by Deo et al. [78].

References

[1] Tipper CF. Metallurgia 1949;39:133.
[2] Dodd B, Bai Y. Ductile fracture and ductility. New York: Academic Press; 1987. p. 97.
[3] Gurson AL. J Eng Mater Tech 1977;99:2.
[4] Needleman A, Tvergaard V. J Mech Phys Solids 1984;32:461.
[5] Tvergaard V, Needleman A. Acta Mater 1984;32:157–69.
[6] Potirniche GP, Hearndon JL, Horstemeyer MF, Ling XW. Int J Plasticity 2006;22:921.
[7] Stevens AL, Davison L, Warren WE. J Appl Phys 1972;43:4922.
[8] Meyers MA, Aimone CT. Prog Mater Sci 1983;28:1.
[9] Wolfer WG. Phil Mag A 1988;48:285.
[10] Ahn DC, Sofronis P, Kumar M, Belak J, Minich RJ. Appl Phys 2007;101:063514-1-6.
[11] Lubarda VA, Schneider MS, Kalantar DH, Remington BA, Meyers MA. Acta Mater 2004;53:1397.

[12] Ashby MF. Phil Mag 1970;21:399.
[13] Ashby MF. In: Kelly A, Nicholson RB, editors. Strengthening Methods in Crystals. Amsterdam: Elsevier; 1971. p. 137.
[14] Seppälä ET, Belak JF, Rudd RE. Phys Rev B 2004;69:134101-1–134101-19.
[15] Seppälä ET, Belak JF, Rudd RE. Phys Rev Lett 2004;93:245503-1-4.
[16] Seppälä ET, Belak JF, Rudd RE. Phys Rev B 2005;71:064112-1–064112-10.
[17] Traiviratana S, Bringa EM, Benson DH, Meyers MA. Acta Mater 2008;56:3874.
[18] Meyers MA, Traiviratana S, Lubarda VA, Benson DJ, Bringa EM. J Mater 2009;61:35–41.
[19] Marian J, Knap J, Ortiz M. Phys Rev Lett 2004;93:165503.
[20] Marian J, Knap J, Ortiz M. Acta Mater 2005;53:2893.
[21] Dávila LP, Erhart P, Bringa EM, Meyers MA, Lubarda VA, Schneider MS, et al. Appl Phys Lett 2005;86:161902.
[22] Zhu W, Song Z, Deng X, He H, Cheng X. Phys Rev B 2007;75:024104-1.
[23] Bringa EM, Traiviratana S, Meyers MA. Acta Mater 2010;58:4458–77.
[24] Bulatov VV, Wolfer WG, Kumar M. Scripta Mater 2010;63:144–7.
[25] Bringa EM, Lubarda VA, Meyers MA. Scripta Mater 2010;63:148–50.
[26] Rudd RE, Belak JF. Compos Mater Sci 2002;24:148–53.
[27] Dongare AM, Rajendran AM, LaMattina B, Zikry MA, Brenner DW. Phys Rev B 2009;80:104108.
[28] Rudd RE. Phil Mag 2009;89:3133–61.
[29] Finnis M, Sinclair J. Phil Mag A 1984;50:45.
[30] Marian J, Knap J, Campbell GH. Acta Mater 2008;56:2389–99.
[31] Duesbery MS, Vitek V. Acta Mater 1998;46:1481–92.
[32] Gröger R, Bailey AG, Vitek V. Acta Mater 2008;56:5401–11.
[33] Gröger R, Racherla V, Bassani JL, Vitek V. Acta Mater 2008;56:5412–25.
[34] Gröger R, Vitek V. Phil Mag 2009;89:3163–78.
[35] Seeger A. Z Metallkd 2002;93:760–77.
[36] Cuitiño AM, Ortiz M. Acta Mater 1996;44:427–36.
[37] Seitz F. Adv Phys 1952;1:43.
[38] Mott NF. Phil Mag 1952;43:1151.
[39] Mott NF. Phil Mag 1953;44:187.
[40] Mott NF. Phil Mag 1953;44:742.
[41] Li YH, Siegel DJ, Adams JB, Liu XY. Phys Rev B 2003;67:125101.
[42] Hodkin EN, Nicholas MG, Poole DM. J Less-Common Met 1970;20:93–103.
[43] Weiler D, Maier K, Mehrer H. In: Kedves FJ, Beke DL, editors. Diffusion in metals and alloys. Zurich: Trans Tech Publications; 1983. p. 342.
[44] Raj R, Ashby MF. Acta Metal 1975;23:653–66.
[45] Argon AS, Im J, Safoglu R. Metal Trans A 1975;6A:825–37.
[46] Puttick KE. Phil Mag 1959;4:964–9.

[47] Rogers HC. AIME Trans 1960;218:498–506.
[48] Edelson B, Baldwin W. Trans ASM 1962;55:230.
[49] Chin GY, Hosford Jr WF, Backofen WA. Trans Met Soc AIME 1964;230:437–49.
[50] Argon AS, Maloof SR. Acta Met 1966;14:1463–8.
[51] Broek D. Elementary engineering fracture mechanics. 3rd rev. ed. The Hague: Martinus Nijhoff; 1982. p. 39.
[52] Kanel GI, Razorenov SV, Fortov VE. In: Meyers MA, Murr LE, Staudhammer KP, editors. Shock-wave and high-strain-rate phenomena in materials, New York: Marcel Dekker; 1992. p. 775.
[53] Rosi FD, Abrahams MS. Acta Met 1960;8:807–8.
[54] Plimpton SJ. J Compos Phys 1995;117:1.
[55] Dai XD, Kong Y, Li JH, Liu BX. J Phys: Condens Matter 2006;18:4527–42.
[56] Ackland GJ, Thetford R. Phil Mag A 1987;56:15.
[57] Liu ZL, Cai LC, Chen XR, Jing FQ. Phys Rev B 2008;77:024103.
[58] Humphrey W, Dalke A, Schulten K. J Mol Graphics 1996;14:33–8.
[59] Tsuzuki H, Branicio PS, Rino JP. Comput Phys Comm 2007;177:518.
[60] Kelchner CL, Plimpton SJ, Hamilton JC. Phys Rev B 1998;58:11085.
[61] Marian J, Cai W, Bulatov VV. Nat Mater 2004;3:158.
[62] Meyers MA, Vohringer O, Lubarda VA. Acta Mater 2001;49:4025–39.
[63] Meyers MA, Schneider MS, Jarmakani H, Kad B, Remington BA, Kalantar DH, et al. Metall Mater Trans A 2008;39A:304–24.
[64] Jarmakani HN, Bringa EM, Erhart P, Remington BA, Wang YM, Vo NQ, et al. Acta Mater 2008;56:5584–604.
[65] Murr LE, Meyers MA, Niou CS, Chen YJ, Pappu S, Kennedy C. Acta Mater 1997;45:157–75.
[66] Zerilli FJ, Armstrong RW. J Appl Phys 1990;68:1580–91.
[67] Hoge KG, Mukherjee AK. J Mater Sci 1977;12:1666.
[68] Rittel D, Silva ML, Poon B, Ravichandran G. Mech Mater 2009;41:1323–9.
[69] Lu CH, Remington BA, Maddox BR, Kad B, Park HS, et al. submitted for publication.
[70] Sherwood PJ, Guiu F, Kim HC, Pratt PL. Can J Phys 1967;45:1075–89.
[71] Gröger R, Vitek V. Acta Mater 2008;56:5426–39.
[72] Greer JR, Weinberger CR, Cai W. Mater Sci Eng A 2008;493:21–5.
[73] Hsiung LM, Lassila DH. Acta Mater 2000;48:4851.
[74] Wang GF, Strachan A, Cagin T, Goddard III WA. Phys Rev B 2003;68:224101.
[75] Mishin Y, Lozovoi AY. Acta Mater 2006;54:5013–26.
[76] Yang LH, Söderlind P, Moriarty JA. Phil Mag 2001;81:1355–85.
[77] Van SH, Derlet PM, Froseth AG. Nat Mater 2004;3:399–403.
[78] Deo CS, Srolovitz DJ, Cai W, Bulatov VV. J Mech Phys Solid 2005;53:1223–47.
[79] Jin ZH, Gao HJ, Gumbsch P. Phys Rev B 2008;77:094303.
[80] Gumbsch P, Gao H. Science 1999;283:965–8.